Abstract

The quantification of cross-regional interactions for the atmospheric transport processes is of crucial importance to improve the predictive capacity of climatic and environmental system modeling. The dynamic interactions in these complex systems are often nonlinear and non-separable, making conventional approaches of causal inference, such as statistical correlation or Granger causality, infeasible or ineffective. In this study, we applied an advanced method, based on the convergent cross mapping algorithm, to detect and quantify the causal influence among different climate regions in the contiguous U.S. in response to temperature perturbations using the long-term (1901–2018) climatology of near surface air temperature record. Our results show that the directed causal network constructed by convergent cross mapping algorithm, enables us to distinguish the causal links from *spurious* ones rendered by statistical correlation. We also detect that the Ohio Valley region, as an atmospheric convergent zone, acts as the regional gateway and mediator to the long-term thermal environments in the U.S. In addition, the temporal evolution of dynamic causality of temperature exhibits superposition of periodicities at various time scales, highlighting the impact of prominent low frequency climate variabilities such as El Niño–Southern Oscillation. The proposed method in this work will help to promote novel system-based and data-driven framework in studying the integrated environmental system dynamics.

Keywords:

Causality; Complex network; Convergent cross mapping; System dynamics; Thermal environment

1. Introduction

The Earth's environment and climate systems involve complex dynamic processes that are non-separable, interacting, and more importantly, have causal influences toward one another. Prominent examples include the drought patterns in the western U.S. that are strongly regulated by the sea surface temperature (SST) of the Pacific (Namias, 1983), the long-distant links (aka teleconnections) between ground level temperature and atmospheric Rossby waves (Wang et al., 2013), and the correlation between anomalous atmospheric circulation and sea ice concentration (Handorf et al., 2015), to name a few. Conventionally, the spatial or inter-variable correlations in the climate system has been established by statistical regression of observational time series or dissimilarity functions via information transfer (e.g., Moran, 1953; Fitzpatrick & Dunn, 2019; Wang et al., 2020a).

On the other hand, successful identification of the directed dynamical influence, viz. *causality*, in Earth's climate system will greatly enhance the modeling and predictive capacity of physically based Earth modeling frameworks (Runge et al., 2015, 2019; Jiang et al., 2016; Leng et al., 2020; Huang et al., 2021). However, the conventional statistical correlation-based methods to infer causality may induce *spurious* links that correlate climate variables driven by the same external forcing but without mutual causal influence (Moran, 1953). These ephemeral or "mirage" correlations (false causality) are common in nonlinear systems. Their presence can lead to incorrect and even contradictory hypotheses (Sugihara et al., 2012), which can impede our understanding of true interactions among system dynamics. In particular, inferring causality from statistical correlation is risky for the Earth's climate system that involves nonlinear dynamics with weak and moderate interactions (McCann et al., 1998). The nonlinearity of climate dynamics, especially the temperature evolution, has been extensively studied in response to, e.g.

different CO_2 emission scenarios (Good et al., 2015), which is largely attributed to the nonlinear albedo feedback such as the sea-ice albedo feedbacks (Hall, 2004; Ishizaki et al., 2012). Furthermore, our previous analysis of long-term temperature anomalies show that the time series exhibit significant increase in autocorrelation and variance prior to critical transitions that features nonlinear dynamic systems (Wang et al., 2020b).

In the literature, the Granger causality (GC) scheme has been commonly used for causal inference, with the key assumption that a variable is causative to a dynamic system if the prediction skill increases by adding this variable to the system's autoregressive processes (Granger, 1969). GC analysis has been applied to climate sciences, examples including the potential causality between El Niño–Southern Oscillation (ENSO) and temperature and wind patterns across the mid-to-high latitudes (McGraw & Barnes, 2018). More recently, Silva et al. (2021) identified GC-based climate teleconnections between the precipitation response to SST and ENSO. Nevertheless, there are some intrinsic disadvantages in GC-based causality analysis, especially the requirement of strong coupling and separability of system dynamics. These assumptions often lead to the loss of feasibility of GC's causality inference, especially in the Earth's climate system where nonlinearity, weakly or moderately coupled dynamics, and nonseparability prevail (Ancona et al., 2004). To overcome the inherited limitation of the GC approach, Sugihara et al. (2012) developed a new method of causal inference based on the convergent cross mapping (CCM) algorithm. The CCM method and its variations (e.g. partial cross mapping, see Runge et al., 2015; Leng et al., 2020) have been successfully applied to detect dynamic causality in Earth's climate system, such as the causal influence of greenhouse gas concentration and midlatitude circulation on global climate changes (van Nes et al., 2015), and the detection of atmospheric teleconnections in monsoon dynamics (Runge et al., 2015). In

addition, causal inference methods have been evaluated in the study of hydrometeorological systems (Wang et al., 2018; Ombadi et al., 2020). In particular, Shi et al. (2022) proposed a new perspective to use causality to detect the drought propagation, in contrast to the overuse of correlation analysis.

In this study, we apply the CCM method to quantify the causal influence in temperature perturbations among different climate regions in the contiguous U.S. (CONUS), using the long-term temperature climatology in 1901–2018. The detection of cross-regional causal interactions can provide new insights to understanding the response of thermal environments (and associated atmospheric transport) to emergent anomalous climatic patterns, with implications to occurrence of extreme events such as mega-heatwaves or persistent droughts. Our analysis also enables us to identify key climate regions, viz. mediators, as critical atmospheric gateways in spreading and distributing climate perturbations, by constructing the CONUS climate system as a complex network. The construction of the causal network, in turn, will facilitate the imperative need of the development of data-driven and system-based frameworks in the integrated Earth system (Fan et al., 2020; Wang & Wang, 2020; Wang, 2021, 2022).

2. Methods

2.1 Data retrieval and treatment

In this study, we retrieved the monthly mean near-surface temperature over the period 1901–2018 from Climatic Research Unit (CRU) Time-Series (TS) version 4.03 (https://catalogue.ceda.ac.uk/uuid/10d3e3640f004c578403419aac167d82) produced by the Center for Environmental Data Analysis (CEDA) Archive. The $0.5^{o} \times 0.5^{o}$ spatially gridded dataset covers the spatial domain of global land surfaces except Antarctica, with a total number

of 3288 grid cells over the entire CONUS. The observational data are anomalized using 1961–1990 monthly averages for each grid cell (Harris et al., 2020). We aggregated all CONUS grid cells into nine climatic regions, to better represent the thermal environments in individual regions with distinct background climatic and geographic conditions. These climatic regions are Northwest (NW), West (WE), Southwest (SW), Northern Rockies and Plains (NRP), South (SO), Upper Midwest (UM), Ohio Valley (OV), Southeast (SE), and Northeast (NE). The division of climate regions is defined by the National Centers for Environmental Information of NOAA (https://www.ncdc.noaa.gov/monitoring-references/maps/us-climate-regions.php). We then removed the seasonal cycle by subtracting monthly anomalies averages from the regional temperature anomalies time series during the study period to minimize the impact of seasonality. The detrended time series of temperature anomalies are used for subsequent causality analysis.

2.2 The convergent cross-mapping CCM method to estimate causality

The CCM method has been developed to detect and quantify the directed causal influence among key parameters in nonlinear dynamic systems, based on the embedding theory (Sugihara et al., 2012). The fundamental concept of the CCM algorithm is that if causality exists between a pair of generic variables, represented by vectors (adequately long time series) X and Y, then we can reconstruct the cross-mapping dynamics of one variable from the information of the other. The reconstruction of phase space for each dynamical variable is based on the delay-coordinate embedding method (Takens, 1981). In addition, CCM uses simple projection (Sugihara & May, 1990), i.e. a nearest-neighbor algorithm that involves exponentially weighted distances from nearby points on a reconstructed manifold, to make kernel estimation.

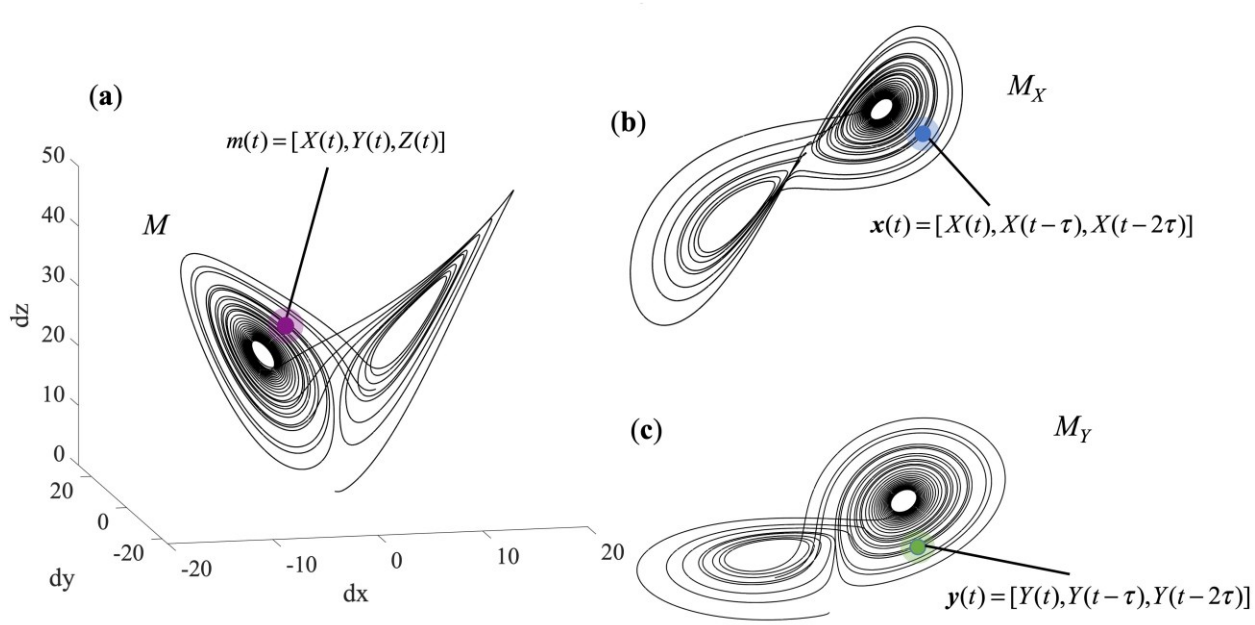

Figure 1. Illustration of correspondence between two shadow manifolds of convergent cross mapping: (**a**) the canonical Lorenz system *m* with three coupled vectors *X*, *Y*, and *Z*, with two attractors projected onto the manifolds of (**b**) M_X and (**c**) M_Y.

For a dynamically coupled canonical Lorenz system, the CCM algorithm is illustrated in Fig. 1, where the reconstructed lagged-coordinate vector for time series $X(t)$ with length L is denoted as $\boldsymbol{x}(t) = [X(t), X(t-\tau), \ldots, X(t-(E-1)\tau)]$, with τ and E the time delay and embedding dimension to construct the shadow manifold M_X, respectively (likewise for $\boldsymbol{y}(t)$ and M_Y). The embedding dimension E can be physically interpreted as the complexity of the state variable (in our case, temperature) as to be causally influenced by other confounding variables in the complex system. For example, it is found that causal analysis of precipitation requires a much larger embedding dimension that that of temperature, indicating the physics of precipitation is of higher complexity than that of heat transfer. In addition, the time delay $\tau = 1$ is equivalent to use consecutive data points in the data series (without filtering) to construct shadow manifolds based

129 on the delay-coordinate embedding. The shadow manifold, constructed using these parameters,
130 represents the low-dimensional approximations of the true system that could be of infinitely high
131 dimension in theory. Thus, the convergence of the CCM method will be limited by observational
132 error, process noise, and time-series length L, e.g. with limited or noisy field data, the
133 predictability of CCM is demonstrated to increases with L.

134 If two generic variables X and Y are causally coupled in a complex system, there is a
135 cross-mapping correspondence between the two attractor manifolds M_X and M_Y. For the given
136 time series $Y(t)$, its cross-mapping estimate $Y(t)|M_X$ is based on a simple projection of the E+1
137 nearest neighbors of vector $\boldsymbol{x}(t)$ in the manifold of M_X, where E+1 is the minimum number of
138 points required for a bounded simplex in the E-dimensional space. The time indices of those E+1
139 neighbors $\boldsymbol{x}(t_1)$, $\boldsymbol{x}(t_2)$,…, $\boldsymbol{x}(t_{E+1})$ (from closest to farthest) in M_X are used to identify the
140 corresponding putative neighbors in Y, i.e. $Y(t_1)$, $Y(t_2)$,…, $Y(t_{E+1})$. The cross-mapping estimate of
141 $Y(t)$, denoted as $Y(t)|M_X$, is determined using the weighted average as

142 $$\hat{Y}(t) \mid M_X = \sum_{i=1}^{E+1} w_i(t) \cdot Y(t_i), \tag{1}$$

143 where the weight vector $w_i(t)$ is estimated by

144 $$w_i(t) = \frac{u_i(t)}{\sum_{j=1}^{E+1} u_i(t)}, \tag{2}$$

145 with

146 $$u_i(t) = \exp\left\{-\frac{d[x(t), x(t_i)]}{d[x(t), x(t_1)]}\right\}, \tag{3}$$

147 and $d[x(t), x(t_i)]$ the Euclidean distance between the two vectors $x(t)$ and $x(t_i)$ in M_X. To measure
148 the causality from Y to X, the correlation coefficient $\rho_{Y|M_X}$ between the original $Y(t)$ and the
149 cross-mapping estimate $\hat{Y}(t)\,|\,M_X$ will be used, which is defined by

150 $$\rho_{Y|M_X} = \frac{\mathbf{E}\left\{\left[Y(t)-\mu_Y\right]\cdot\left[\hat{Y}(t)\,|\,M_X-\mu_{\hat{Y}}\right]\right\}}{\sigma_Y\sigma_{\hat{Y}}}, \quad (4)$$

151 where **E**, μ, and σ are the statistical expectation, average, and standard deviation, respectively.
152 The larger value implies a stronger casual influence, while Y is not causal to X if $\rho_{Y|M_X} \le 0$.

153

154 *2.3 Time delay and embedding dimension to reconstruct phase-space dynamical system*

155 Since the CCM method is derived from the standard delay-coordinate embedding method
156 (Takens, 1981), the phase space of the underlying dynamical system can be reconstructed from
157 time series and the accuracy of the reconstruction requires the proper choice of the time delay τ
158 and the embedding dimension E. The value of the time delay can be computed as the
159 autocorrelation length (Kantz, 1997). Empirically, the delay time can be chosen as the average
160 oscillation period of the underlying times series, that is corresponding to unit value in discrete-
161 time map (Lai & Ye, 2003; Grassberger & Procaccia, 1983; 2004). Thus, for temperature
162 anomaly here the time delay is chosen as $\tau = 1$. The properly chosen embedding dimension E can
163 be determined using the correlation integral and dimension method or the GP-algorithm
164 (Grassberger & Procaccia, 1983; Lai & Ye, 2003). The correlation dimension D_2 in nonlinear
165 time series can be evaluated by using the correlation integral $C(\varepsilon)$, which is the probability that a
166 pair of points chosen randomly in the reconstructed phase space is within a hypersphere of radius
167 ε (Grassberger & Procaccia, 1983; Lai & Ye, 2003). For the reconstructed vector time series $\boldsymbol{x}(t)$
168 with number of points N inside, the correlation integral can be approximated by

$$C_N(\varepsilon) = \frac{1}{N(N-1)} \sum_{j=1}^{N} \sum_{i=j+1}^{N} \Theta\left(\varepsilon - \left\|\boldsymbol{x}_i - \boldsymbol{x}_j\right\|\right), \tag{5}$$

where Θ is the Heaviside step function, and $\left\|\boldsymbol{x}_i - \boldsymbol{x}_j\right\|$ is the distance between $\boldsymbol{x}_i$ and $\boldsymbol{x}_j$. The correlation dimension D_2 is given by consequently

$$D_2 = \lim_{\varepsilon \to 0} \lim_{N \to \infty} \frac{\log C_N(\varepsilon)}{\log \varepsilon}. \tag{6}$$

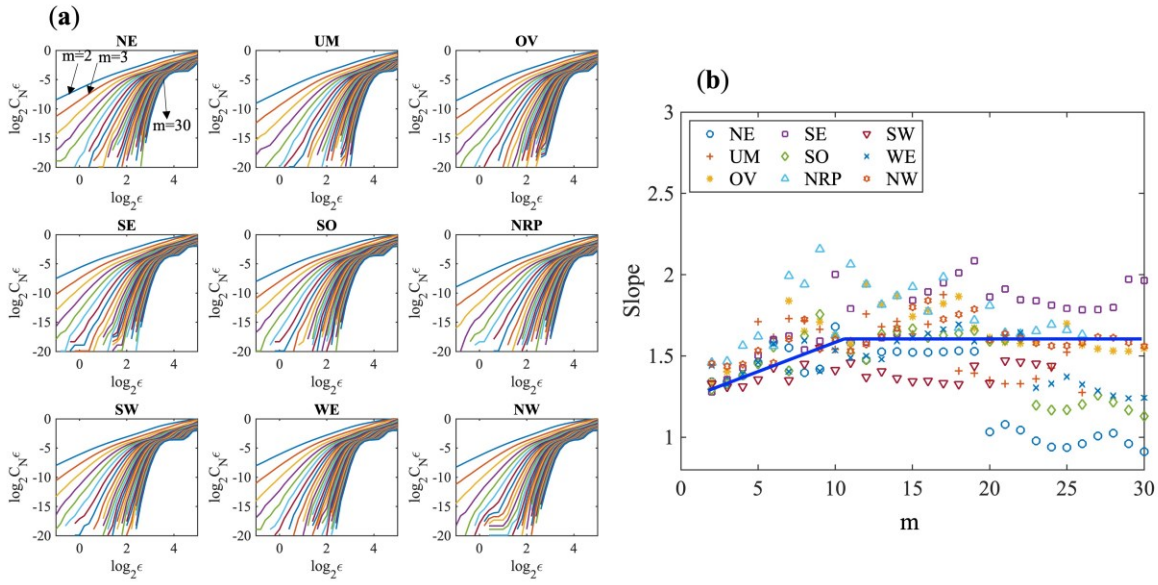

Figure 2. Determination of the embedding dimension E using the GP-algorithm of correlation integral and dimension from the aggregated time series of regional temperature anomalies: (**a**) plots of the correlation integral on a logarithm scale for different embedding dimension m = 1, …, 30 for the nine climate regions, and (**b**) the slope values of $\log C_N(\varepsilon)$ versus $\log \varepsilon$ for the nine climate regions obtained from a least-squares fitting. The slope increases with m and reaches an approximate plateau value, as shown by the two blue solid lines for eye guidance.

In practice, the correlation dimension D_2 is estimated by examining the slope of the linear portion of $\log C_N(\varepsilon)$ versus $\log\varepsilon$ for a series of increasing values of m (different embedding dimensions). Results of detailed calculations of the correlation integrals and correlation dimension from the aggregated time series of temperature anomalies are shown in Fig. 2. The slope in the plot increases with m until it reaches a plateau and the slope value at the plateau is then taken as the D_2 estimation (Grassberger & Procaccia, 1983; Ding et al., 1993). The results show the D_2 estimation is around 1.7, the embedding dimension E for the reconstruction must be sufficiently large as for an infinite, noiseless time series, the estimated dimension value D_2 increases with E but plateaus for $E > [\overline{D_2}] + 1$ (Ding et al., 1993), so the embedding dimension is determined as $E = 3$.

2.4 The regional causal effect and causal susceptibility

The aforementioned algorithm enables us to quantify the directed causality between the temperature anomalies in each pair of climate regions, resulted in a directed causal *network* of temperature climatology in CONUS with nine nodes, each representing one climate region. Using this network, we define two indices to measure the causal effect and causal sensitivity for a climate region: the average causal *effect* (*ACE*) and the average causal *susceptibility* (*ACS*). The estimate of *ACE* and *ACS* for a given region R can be calculated by averaging along individual column and rows of the adjacency matrix of the causality network, respectively (Runge et al., 2015):

$$ACE_R(t) = \frac{1}{N_R - 1}\sum_{i \neq R} \rho_{X_R(t)|M_i}\,, \tag{7}$$

$$ACS_R(t) = \frac{1}{N_R - 1} \sum_{i \neq R} \rho_{X_i(t)|M_R}, \quad (8)$$

where N_R is the total number of climate regions. Furthermore, to investigate the long-term trend of *ACE* and *ACS*, we compute their running averages using a sliding window of size w, as for a time window [k-(w-1)/2, k+(w-1)/2], with k at the middle of the time window, as

$$\overline{ACE}_{R,k} = \frac{1}{w} \sum_{j=k-(w-1)/2}^{k+(w-1)/2} ACE(j), \quad (9)$$

$$\overline{ACS}_{R,k} = \frac{1}{w} \sum_{j=k-(w-1)/2}^{k+(w-1)/2} ACS(j). \quad (10)$$

In a given region R, a larger *ACE* value means a stronger causal effect of that region to mediate the thermal climatology in other regions. Likewise, a higher *ACS* value signifies that the region is more susceptible to thermal perturbations of other regions.

3. Results and Discussion

3.1 Statistical correlation vs. causality

We first constructed a directed causal network of the temperature climatology among the nine CONUS climatic regions, using the CCM algorithm outlined in Section 2. The inter-regional interactions of climatic variables have been quantified using conventional statistical similarity functions or Granger causality methods that directly link the time series of climatic variables between a pair of nodes (Boers et al., 2019; Fitzpatrick & Dunn, 2019; Silva et al., 2021). In this study, in addition to CCM analysis, we also constructed an *undirected* CONUS regional network using statistical correlation coefficient, defined in Eq. (4) but between the observed $X(t)$ (instead of cross-mapping estimate) and $Y(t)$ directly.

Figure 3 shows the comparison of the undirected correlation (Fig. 3**a**) and directed causality (Fig. 3**b**) networks. It is noteworthy that the network of statistical correlations is stronger than the causal counterpart, as manifested by the darker color in Fig. 3**a** representing higher strength. By definition, the correlation network is symmetric and without directionality. In comparison, the directed causal network is generally asymmetric, as the causal influence from X to Y is not necessarily the same as that from Y to X. In this specific case, however, the causality network of CONUS temperature climatology (Fig. 3**b**) is rather (not completely though) symmetric, suggesting the cross-regional causal influence among CONUS climate regions is, in general, reciprocated in terms of the atmospheric heat transfer. For example, the temperature in the OV region exerts a causal influence on four neighboring regions (NE, UM, SE, SO) with strength greater than 0.6, while the latter regions responded with a mutual causal effect with comparable strength. The cause-effect network of temperature in Fig. 3**b** is sparser (with less number of connectivities) than the one from the simple correlations in Fig. 3**a**, because the latter often admits spurious links due to common external variables (Shi et al., 2022; Sugihara et al., 2012).

To facilitate a more direct comparison of the statistical correlation and causality, we identified the effect links in the networks using a common threshold value of 0.5. The choice of this threshold is adopted from the suggested value by previous studies (Tsonis and Roebber, 2004; Yang et al., 2022), which has been tested to be statistically significant. A pair of climate regions is considered as effectively connected (statistically or causally) if the strength in matrices of Fig. 3**a** and 3**b** is greater than 0.5. The choice of this threshold value follows previous study of thermal climate network and was validated by statistical test (Tsonis & Roebber, 2004; Wang et al., 2021). The results are shown in Fig. 3**c**, where the links with significant statistical correlation

but no causality are marked as *spurious* links and represented by gray dash lines. In this case, we identified three spurious links, namely that connect SW and NRP, SW and SO, and SO and UM.

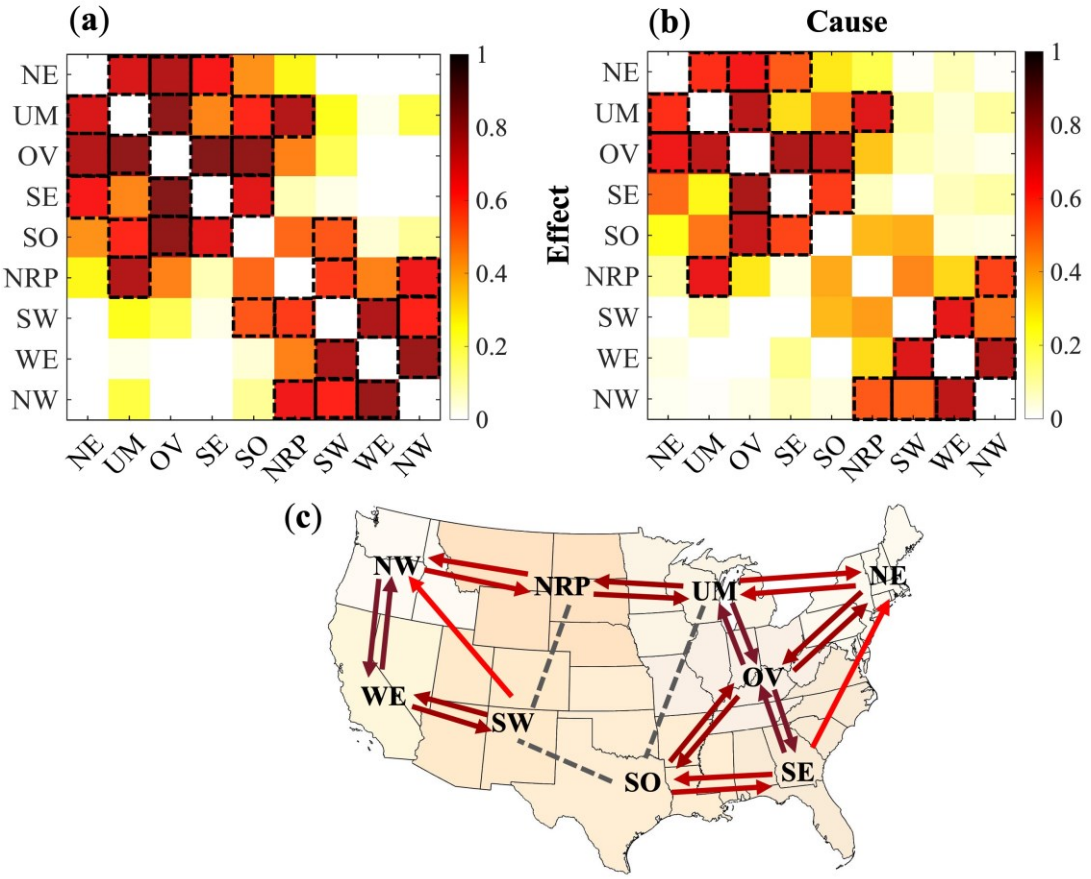

Figure 3. Comparison of the correlation and causality networks for the nine CONUS climate regions: (**a**) the matrix of connectivity determined by undirected statistical correlation, (**b**) the matrix of connectivity determined by directed causality, and (**c**) graphic representation of causal and spurious links resulted from (**a**) and (**b**), with a threshold strength of 0.5. Cells with dashed boxes in (**a**) and (**b**) represent causally (above the threshold) connected pairs. The gray dashed lines represent the spurious link between different regions, and lines with an arrow the directed causal influence with strength denoted by different colors (the same scale as in (**b**)).

The number of spurious links is seemingly small, but the implication is significant. First, the South and Southwest regions stand out as most significantly affected by spurious links, likely due to the analogy in thermal environments that subject to common radiative forcing. Secondly, by removing the spurious links in Fig. 3**c**, the southern part of the CONUS thermal climate network is effectively a bipartite system with distinct east and west clusters. The emergence of clustering in CONUS climate network is consistent with the finding in a previous study based on advanced information theory (Wang et al., 2020a). More specifically, in the east half of the CONUS network, the Ohio Valley region appears to be the gateway of cross-regional thermal interactions. This is not only due to the geographic location of the region, but also agrees with climatic observations and modeling results as reported in the literature as well (detailed below in Section *3.2*).

In addition, we also constructed the causal graphs using the GC approach. The results are shown in Figs. A1 and A2 in Appendix. It can be seen that the causality networks detected by GC, though self-consistent, are at variance with and not comparable to those detected by CCM or conventional statistical correlation (Figs. 3a,b). This discrepancy can be attributed to that the GC method is: (1) not most fitful for nonlinear systems with moderate coupling, and (2) very sensitive to the choice of maximum delay τ_{max} to do the autoregression analysis, the determination of which can be rather arbitrary and does not admit a solid physical interpretation.

3.2 Regional causal effect and susceptibility

We then further investigate the causal network and quantify the role of each climate region in transporting and distributing temperature perturbations. It was found that regions with strong strength in causal effect and/or susceptibility are linked with major atmospheric uplifting

zones in complex climate systems (Runge et al., 2015). The results of calculated *ACE* and *ACS* indices, as defined in Eqs. (7) and (8) and averaged over the entire study period, are shown in Fig. 4, mapped over CONUS. It is clear that the Ohio Valley region acts as a causal gateway and mediator at the same time, manifested as the brightest region (i.e. with highest values of *ACE* and *ACS*). This means that the Ohio Valley is the most conducive to spreading temperature anomalies (e.g. heat extremes) to (Fig. 4**a**), meanwhile the most susceptible to thermal perturbations arising from (Fig. 4**b**) other regions in CONUS. Potential physical mechanisms that contribute to making OV a regional gateway include: (a) this region has the strongest geostrophic wind components (Walsh et al., 1982); (b) it is most significantly affected by ENSO and temperature extremes (Gershunov & Barnett, 1998); and (c) it mediates atmospheric heat transfer and drought distribution in the U.S. with high climate variability (Karl & Koscielny, 1982; Konapala & Mishra, 2017; Zhang et al., 2010).

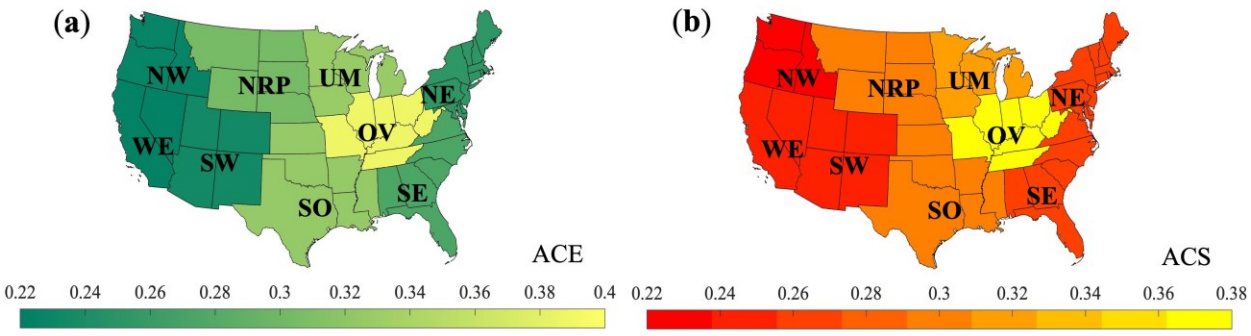

Figure 4. Quantification of (**a**) the average causal effect and (**b**) the average causal susceptibility for the temperature climatology in CONUS. The colors correspond to the causal effect or susceptibility strength.

In the western U.S., the NW, WE, and SW regions, in general, have weaker local causal influence than their eastern counterparts. Nevertheless, due to the presence of long-range

connectivity among CONUS climate regions, the susceptibility of the Great Plains to climatic extremes, e.g. summer drought and heatwaves, could also be regulated by the Pacific oceanic conditions. For example, Namias (1983) found that in the West, the local surface circulation is characterized by easterly wind anomalies that are originated from the continental interior and mostly directed down the slope of the Rocky Mountain Ridge (Lau & Nath, 2012). The western ridges therefore contribute to build *blocking* high pressure systems to cyclonic activity from the Pacific. As a consequence, the development of a North Pacific oscillation (NPO) exerts a causally dynamic influence on the atmospheric transport of heat and moisture, in particular storm tracks, as to amplify and stabilize the heat and drought patterns (Charney & DeVore, 1979; Namias, 1983; Matsueda, 2011). This causal influence in climate dynamics is largely responsible for the persistent drought and mega-heatwave episodes over the western U.S. in summers (Perkins, 2015; Wang et al., 2021).

3.3 Temporal variability and periodicity of causality

The dynamics of complex climate system are known to subject to temporal variability ranging from seasonal to millennium time scales (Kenyon & Hegerl, 2008; Ghil & Lucarini, 2020), so does their causal influence. In this study, we further attempt to look into the temporal variability and the presence of possible periodicity in the causal network of CONUS temperature anomalies, by looking into the running means of *ACE* and *ACS* defined in Eqs. (9) and (10). The results are shown in Fig. 5, with a 15-year sliding window size. The time evolution of *ACE* and *ACS* in all the nine climate regions exhibit patterns of superposition of climatic periodicity at different time scales, as expected. The low frequency climatic variability at decadal scale is discernible in the time history, which are likely due to the influence of ENSO or NPO as their

influence is manifested in determining the atmospheric gateways as discussed before (Section 3.2). In particular, the strong correlation between ENSO and the general trend of global temperature changes has been well demonstrated (e.g. Arblaster & Alexander, 2012). It was also found that the Pacific Decadal Oscillation (PDO) has great impacts on the temperature extremes over the northern Pacific Rim and North America (Kenyon & Hegerl, 2008). In addition, it has been tantalizingly suggested that the presence of persistent droughts and heat over the western U.S. may be linked to the double sunspot cycle, with a periodicity of re-occurrence around 20-25 year (Namias, 1983). The western high pressure may be periodically reinforced by downstream strong cyclonic systems from central and eastern North America, and the characteristics of the regional pressure may contribute to the temperature periodicity in western US (Namias, 1983). In the Great Plains region, the low-frequency circulation changes suggest that there exists a prominent mid-tropospheric blocking anticyclone over that region, and these air patterns are in a realignment with the planetary-scale wave structure (Lau & Nath, 2012).

These aforementioned mechanisms of climatic periodicity were, in the literature, mostly observed or explained as statistical correlations, while their causal influence remain obscure up to date. The results in Fig. 5 provide some clue to further unravel the *causal* dynamics in the CONUS climate system. Other than the natural climate variability, the periodicity or cyclicity of causal dynamics has been under-explored up to date. To fully disentangle the various principal modes of the causal variability, it requires further spectral analysis using more sophisticated tools, such as the empirical mode decomposition (EMD) analysis (Huang et al., 1998).

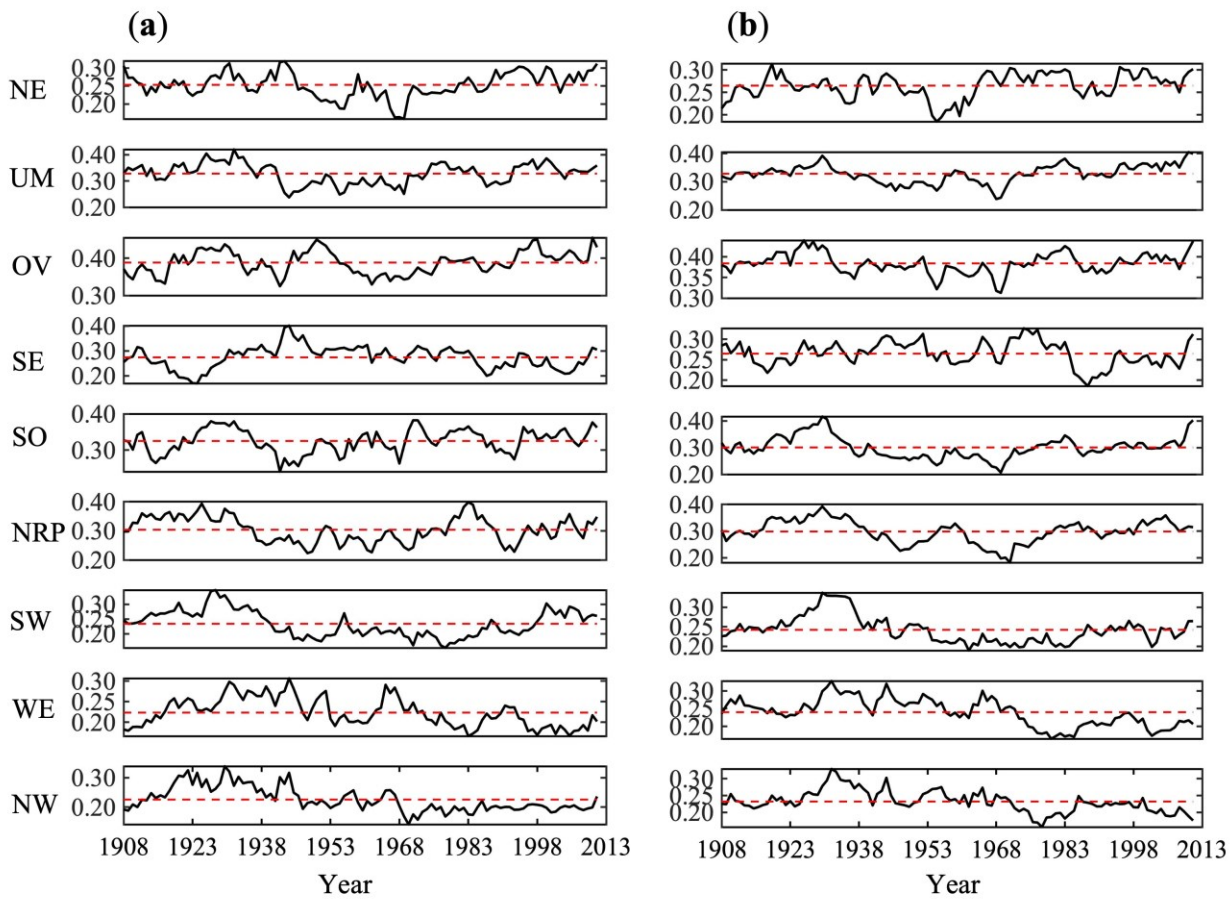

Figure 5. Temporal evolution of the running means of (**a**) *ACE* and (**b**) *ACS* of the causal network for CONUS regional temperature anomalies. A 15-year sliding window size is used, with the red dashed lines denoting the mean values over the entire study period.

4. Concluding Remarks

The spreading of thermal perturbations dictates the atmospheric heat transfer in the Earth system. The data-driven causal inference method CCM provides new insights to identify thermal influence and feedback among the climate regions in CONUS, using the long-term near surface air temperature observations. Our results demonstrate that the conventional statistical method to infer causal relationships may lead to *spurious* links in Earth's climate system that is moderately

coupled. As indicated by the directed causal network, our findings highlight the Ohio Valley as the regional thermal mediator to the temperature perturbations over the CONUS. It is noteworthy that the CCM method can be applied to identify causal relationship between different variables that also contribute to regulating the thermal environment of the U.S., e.g. pressure, wind, soil moisture, etc. Introducing these confounding variables in the causal analysis will enable us to construct more informative (and more complex) causal graphs that vary spatio-temporally and cross pairwise variable. Nevertheless, disentangling and interpretating information in such complex causal graphs present physical and numerical challenges that need to be tackled in future studies; one example of such challenge will be on how to determine the cross-variable embedding dimension E in the CCM method. In future studies, it is important to extend the proposed method to investigate the key role that the major climate oscillations play behind the causality of thermal interactions, and to better understand the physical mechanisms in the occurrence of extreme events such as heatwaves and persistent droughts.

Acknowledgements

This study is based upon work supported by the National Science Foundation (NSF) under Grant # AGS-1930629 and CBET-2028868, and by the National Aeronautics and Space Administrations (NASA) under grant No. 80NSSC20K1263. The authors thank the Associate Editor Dr. Zhiyuan Cong and two anonymous reviewers for their constructive feedback for improving the quality of the paper.

Appendix:

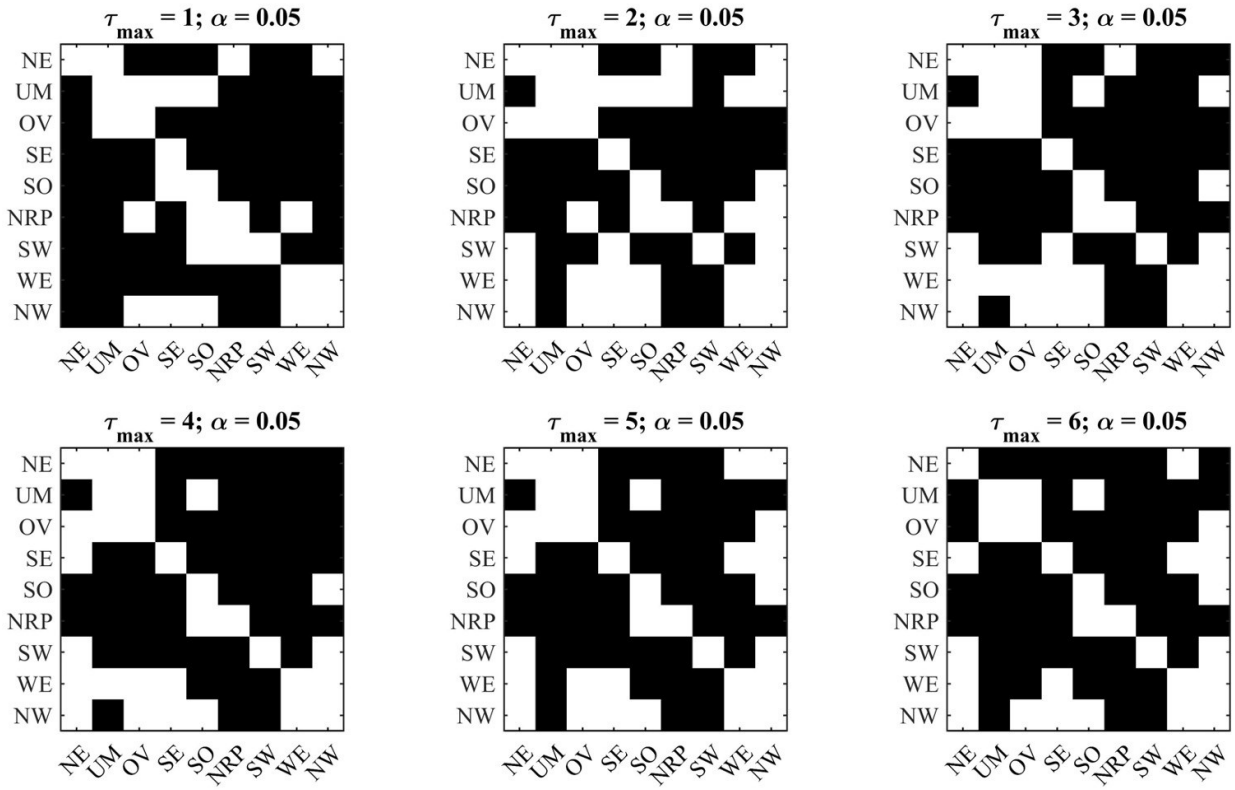

Figure A1. The temperature interactions among the CONUS using Granger Causality method, where τ_{max} is the maximum time delay of the GC autoregression model, and α the significance level. The black cells represent effective causality.

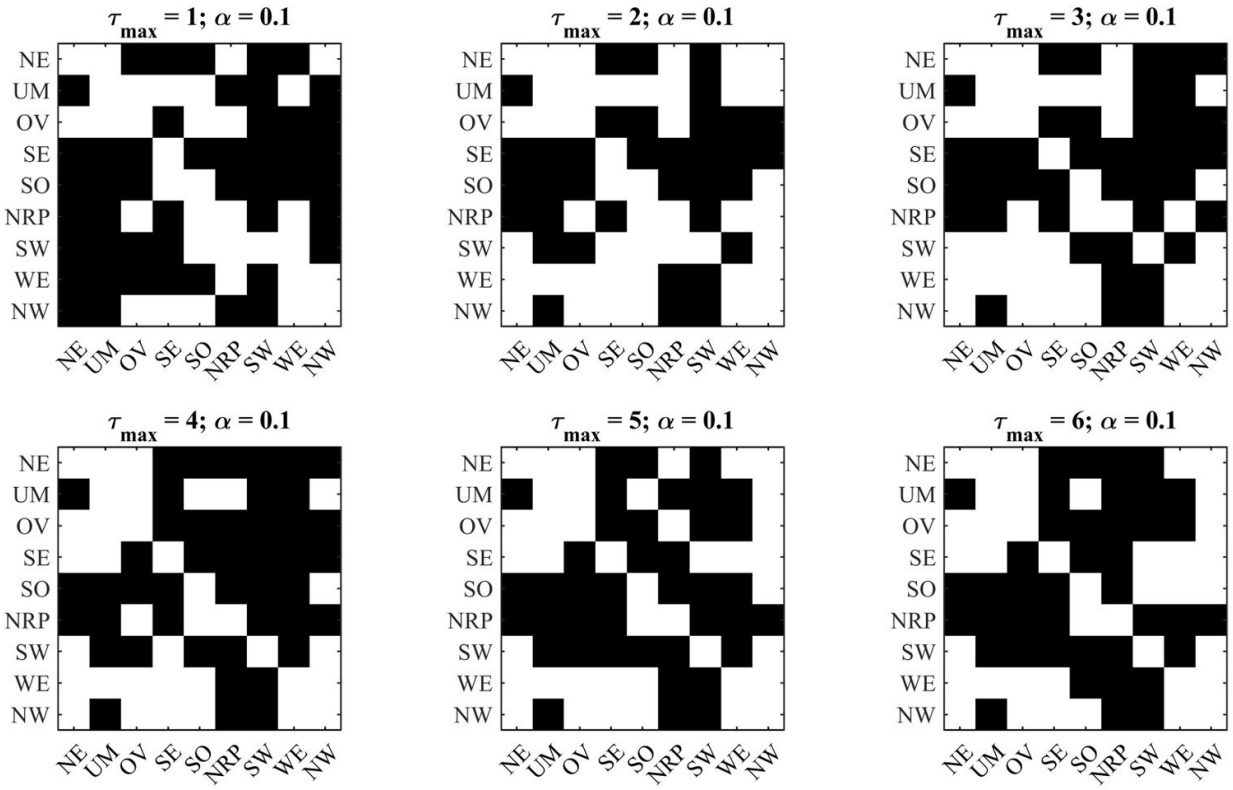

379

380 **Figure A2**. Same with Fig. A1, but with different significance level $\alpha = 0.1$.

References

Ancona, N., Marinazzo, D., & Stramaglia, S. (2004). Radial basis function approach to nonlinear Granger causality of time series. *Physical Review E*, *70*(5), 056221. https://doi.org/10.1103/PhysRevE.70.056221

Arblaster, J. M., & Alexander, L. V. (2012). The impact of the El Niño-Southern Oscillation on maximum temperature extremes. *Geophysical Research Letters*, *39*(20), L20702. https://doi.org/10.1029/2012GL053409

Boers, N., Goswami, B., Rheinwalt, A., Bookhagen, B., Hoskins, B., & Kurths, J. (2019). Complex networks reveal global pattern of extreme-rainfall teleconnections. *Nature*, *566*, 373–377. https://doi.org/10.1038/s41586-018-0872-x

Charney, J. G., & DeVore, J. G. (1979). Multiple flow equilibria in the atmosphere and blocking. *Journal of the Atmospheric Sciences*, *36*(7), 1205–1216. https://doi.org/10.1175/1520-0469(1979)036<1205:MFEITA>2.0.CO;2

Ding, M., Grebogi, C., Ott, E., Sauer, T. & Yorke, J. A. (1993). Plateau onset for correlation dimension: When does it occur? *Physical Review Letters*. 70, 3872–3875. https://doi.org/10.1103/PhysRevLett.70.3872

Fan, J., Meng, J., Ludescher, J., Chen, X., Ashkenazy, Y., Kurths, J., et al. (2020). Statistical physics approaches to the complex Earth system. *Physics Reports*, In press. https://doi.org/10.1016/j.physrep.2020.09.005

Fitzpatrick, M.C., & Dunn, R.R. (2019). Contemporary climatic analogs for 540 North American urban areas in the late 21st century. *Nature Communications*, *10*, 614-617. https://doi.org/10.1038/s41467-019-08540-3

Gershunov, A., & Barnett, T.P. (1998). Interdecadal modulation of ENSO teleconnections. *Bulletin of the American Meteorological Society*, *79*(12), 2715-2725. https://doi.org/10.1175/1520-0477(1998)079<2715:IMOET>2.0.CO;2

Ghil, M., & Lucarini, V. (2020). The physics of climate variability and climate change. *Reviews of Modern Physics*, *92*(3), 035002. https://doi.org/10.1103/RevModPhys.92.035002

Good, P., Lowe, J.A., Andrews, T., Wiltshire, A., Chadwick, R., Ridley, J.K., Menary, M.B., Bouttes, N., Dufresne, J.L., Gregory, J.M., Schaller, N., & Shiogama, H. (2015). Nonlinear regional warming with increasing CO_2 concentrations. *Nature Climate Change 5*, 138–142. https://doi.org/10.1038/nclimate2498

Granger, C. W. (1969). Investigating causal relations by econometric models and cross-spectral methods. *Econometrica*, *37*, 424–438. https://doi.org/1912791

Grassberger, P., & Procaccia, I. (1983). Characterization of strange attractors. *Physical Review Letters*, *50*(5), 346–349. https://doi.org/10.1103/PhysRevLett.50.346

Grassberger, P., Procaccia, I. (2004). Measuring the Strangeness of Strange Attractors. In: Hunt, B.R., Li, TY., Kennedy, J.A., Nusse, H.E. (eds) *The Theory of Chaotic Attractors*. Springer, New York, NY. https://doi.org/10.1007/978-0-387-21830-4_12

Hall, A. (2004). The role of surface albedo feedback in climate. *Journal of Clim*ate *17*, 1550–1568. https://doi.org/10.1175/1520-0442(2004)017<1550:TROSAF>2.0.CO;2

Handorf, D., Jaiser, R., Dethloff, K., Rinke, A., & Cohen, J. (2015). Impacts of Arctic sea ice and continental snow cover changes on atmospheric winter teleconnections. *Geophysical Research Letters*, *42*(7), 2367–2377. https://doi.org/10.1002/2015GL063203

Harris, I., Osborn, T. J., Jones, P., & Lister, D. (2020). Version 4 of the CRU TS monthly high-resolution gridded multivariate climate dataset. *Scientific Data*, *7*(1), 109. https://doi.org/10.1038/s41597-020-0453-3

Huang, N.E., Shen, Z., Long, S.R., Wu, M.C., Shih, H.H., Zheng, Q., Yen, N.-C., Tung, C.C., & Liu, H.H. (1998). The empirical mode decomposition and the Hilbert spectrum for nonlinear and non-stationary time series analysis. *Proceedings of the Royal Society of London. Series A: Mathematical, Physical and Engineering Sciences*, *454*(1971), 903-995. https://doi.org/10.1098/rspa.1998.0193

Huang, Y., Kleindessner, M., Munishkin, A., Varshney, D., Guo, P., & Wang, J. (2021). Benchmarking of data-driven causality discovery approaches in the interactions of Arctic sea ice and atmosphere. *Frontiers in Big Data*, *4*. https://doi.org/10.3389/fdata.2021.642182

Ishizaki, Y., Shiogama, H., Emori, S., Yokohata, T., Nozawa, T., Ogura, T., Abe, M., Yoshimori, M., & Takahashi, K. (2012). Temperature scaling pattern dependence on representative concentration pathway emission scenarios. *Climate Change 112*, 535–546. https://doi.org/10.1007/s10584-012-0430-8

Jiang, J.-J., Huang, Z.-G., Huang, L., Liu, H., & Lai, Y.-C. (2016). Directed dynamical influence is more detectable with noise. *Scientific Reports, 6*(1), 24088. https://doi.org/10.1038/srep24088

Karl, T. R., & Koscielny, A. J. (1982). Drought in the United States: 1895–1981. *Journal of Climatology*, *2*(4), 313–329. https://doi.org/10.1002/joc.3370020402

Kantz, H. & Schreiber, T. (1997). *Nonlinear Time Series Analysis*. Cambridge University Press.

Kenyon, J., & Hegerl, G. C. (2008). Influence of modes of climate variability on global temperature extremes. *Journal of Climate*, *21*(15), 3872–3889. https://doi.org/10.1175/2008JCLI2125.1

Konapala, G., & Mishra, A. (2017). Review of complex networks application in hydroclimatic extremes with an implementation to characterize spatio-temporal drought propagation in continental USA. *Journal of Hydrology*, *555*, 600–620. https://doi.org/10.1016/j.jhydrol.2017.10.033

Kretschmer, M., Coumou, D., Donges, J. F., & Runge, J. (2016). Using causal effect networks to analyze different Arctic drivers of midlatitude winter circulation. *Journal of Climate*, *29*(11), 4069–4081. https://doi.org/10.1175/JCLI-D-15-0654.1

Lai, Y.-C., & Ye, N. (2003). Recent developments in chaotic time series analysis. *International Journal of Bifurcation and Chaos*, *13*(06), 1383–1422. https://doi.org/10.1142/S0218127403007308

Lau, N.-C., & Nath, M. J. (2012). A model study of heat waves over north America: Meteorological Aspects and Projections for the Twenty-First Century. *Journal of Climate*, *25*(14), 4761–4784. https://doi.org/10.1175/JCLI-D-11-00575.1

Leng, S., Ma, H., Kurths, J., Lai, Y.-C., Lin, W., Aihara, K., & Chen, L. (2020). Partial cross mapping eliminates indirect causal influences. *Nature Communications, 11*(1), 2632. https://doi.org/10.1038/s41467-020-16238-0

Matsueda, M. (2011). Predictability of Euro-Russian blocking in summer of 2010. *Geophysical Research Letters*, *38*(6). https://doi.org/10.1029/2010GL046557

McCann, K., Hastings, A., & Huxel, G. R. (1998). Weak trophic interactions and the balance of nature. *Nature*, *395*(6704), 794–798. https://doi.org/10.1038/27427

McGraw, M. C., & Barnes, E. A. (2018). Memory Matters: A case for Granger causality in climate variability studies. *Journal of Climate*, *31*(8), 3289–3300. https://doi.org/10.1175/JCLI-D-17-0334.1

Moran, P. a. P. (1953). The statistical analysis of the Canadian Lynx cycle. *Australian Journal of Zoology*, *1*(3), 291–298. https://doi.org/10.1071/zo9530291

Namias, J. (1983). Some causes of United States drought. *Journal of Applied Meteorology and Climatology*, *22*(1), 30–39. https://doi.org/10.1175/1520-0450(1983)022<0030:SCOUSD>2.0.CO;2

Ombadi, M., Nguyen, P., Sorooshian, S., & Hsu, K. (2020). Evaluation of methods for causal discovery in hydrometeorological systems. *Water Resources Research*, *56*(7), e2020WR027251. https://doi.org/10.1029/2020WR027251

van Nes, E. H., Scheffer, M., Brovkin, V., Lenton, T. M., Ye, H., Deyle, E., & Sugihara, G. (2015). Causal feedbacks in climate change. *Nature Climate Change*, *5*(5), 445–448. https://doi.org/10.1038/nclimate2568

Perkins, S. E. (2015). A review on the scientific understanding of heatwaves—Their measurement, driving mechanisms, and changes at the global scale. *Atmospheric Research*, *164–165*, 242–267. https://doi.org/10.1016/j.atmosres.2015.05.014

Runge, J., Petoukhov, V., Donges, J. F., Hlinka, J., Jajcay, N., Vejmelka, M., et al. (2015). Identifying causal gateways and mediators in complex spatio-temporal systems. *Nature Communications*, *6*(1), 8502. https://doi.org/10.1038/ncomms9502

Runge, J., Nowack, P., Kretschmer, M., Flaxman, S., & Sejdinovic, D. (2019). Detecting and quantifying causal associations in large nonlinear time series datasets. *Science Advances*, *5*(11), eaau4996. https://doi.org/10.1126/sciadv.aau4996

Shi, H., Zhao, Y., Liu, S., Cai, H., & Zhou, Z. (2022). A new perspective on drought propagation: causality. *Geophysical Research Letters*, *49*(2), e2021GL096758. https://doi.org/10.1029/2021GL096758

Silva, F. N., Vega-Oliveros, D. A., Yan, X., Flammini, A., Menczer, F., Radicchi, F., et al. (2021). Detecting climate teleconnections with Granger causality. *Geophysical Research Letters*, *48*(18), e2021GL094707. https://doi.org/10.1029/2021GL094707

Sugihara, G., May, R., Ye, H., Hsieh, C.-H., Deyle, E., Fogarty, M., & Munch, S. (2012). Detecting causality in complex ecosystems. *Science*, *338*(6106), 496–500. https://doi.org/10.1126/science.1227079

Sugihara, G., & May, R. M. (1990). Nonlinear forecasting as a way of distinguishing chaos from measurement error in time series. *Nature*, *344*(6268), 734–741. https://doi.org/10.1038/344734a0

Takens, F. (1981). Detecting strange attractors in fluid turbulence. In D. Rand & L. S. Young (Eds.), *Dynamical Systems and Turbulence* (Vol. 898, pp. 366–381). Berlin: Springer-Verlag. https://doi.org/10.1007/BFb0091924

Tsonis, A.A., & Roebber, P.J. (2004). The architecture of the climate network. *Physica A*, *333*, 497-504. https://doi.org/10.1016/j.physa.2003.10.045

Walsh, J.E., Richman, M.B., & Allen, D.W. (1982). Spatial coherence of monthly precipitation in the United States. *Monthly Weather Review*, *110*(4), 272-286. https://doi.org/10.1175/1520-0493(1982)110<0272:SCOMPI>2.0.CO;2

Wang, C., & Wang, Z. H. (2020). A network-based toolkit for evaluation and intercomparison of weather prediction and climate modeling. *Journal of Environmental Management, 268*, 110709. https://doi.org/10.1016/j.jenvman.2020.110709

514 Wang, C., Wang, Z.H., & Li, Q. (2020a). Emergence of urban clustering among U.S. cities under
515 environmental stressors. *Sustainable Cities and Society*, *63*, 102481.
516 https://doi.org/10.1016/j.scs.2020.102481
517 Wang, C., Wang, Z.H., & Sun, L. (2020b). Early-warning signals for critical temperature
518 transitions. *Geophysical Research Letter 47*, e2020GL088503.
519 https://doi.org/10.1029/2020GL088503
520 Wang, Y., Gozolchiani, A., Ashkenazy, Y., Berezin, Y., Guez, O., & Havlin, S. (2013).
521 Dominant imprint of Rossby waves in the climate network. *Physical Review Letters*,
522 *111*(13), 138501. https://doi.org/10.1103/PhysRevLett.111.138501
523 Wang, Y., Yang, J., Chen, Y., De Maeyer, P., Li, Z., & Duan, W. (2018). Detecting the causal
524 effect of soil moisture on precipitation using convergent cross mapping. *Scientific Reports*,
525 *8*(1), 12171. https://doi.org/10.1038/s41598-018-30669-2
526 Wang, Z.H. (2021). Compound environmental impact of urban mitigation strategies: Co-
527 benefits, trade-offs, and unintended consequence. *Sustainable Cities and Society*, *75*,
528 103284. https://doi.org/10.1016/j.scs.2021.103284
529 Wang, Z.H. (2022). Reconceptualizing urban heat island: Beyond the urban-rural dichotomy.
530 *Sustainable Cities and Society*, *77*, 103581.
531 https://doi.org/https://doi.org/10.1016/j.scs.2021.103581
532 Wang, Z.H., Wang, C., & Yang, X. (2021). Dynamic synchronization of extreme heat in
533 complex climate networks in the contiguous United States. *Urban Climate*, *38*, 100909.
534 https://doi.org/10.1016/j.uclim.2021.100909

Yang, X., Wang, Z.H., & Wang, C. (2022). Critical transitions in the hydrological system: early-warning signals and network analysis. *Hydrology and Earth System Sciences*, *26*(7), 1845-1856. https://doi.org/10.5194/hess-26-1845-2022

Zhang, X., Wang, J., Zwiers, F. W., & Groisman, P. Y. (2010). The Influence of large-scale climate variability on winter maximum daily precipitation over North America. *Journal of Climate*, *23*(11), 2902–2915. https://doi.org/10.1175/2010JCLI3249.1